BUBBLE FORMATION FROM A FLEXIBLE HOLE SUBMERGED IN AN INVISCID LIQUID.

Karine Loubière, Gilles Hébrard*

Laboratoire d'Ingénierie des Procédés de l'Environnement, Département G.P.I., Institut National des Sciences Appliquées,

135 avenue de Rangueil, 31077 Toulouse Cedex 4, FRANCE

Abstract

In the waste water treatment industry, a novel gas sparger based on flexible membranes has been used for the last ten years. The objective of the present work is to study the bubble formation generated from a flexible orifice (membrane). Firstly, the membranes are characterised with regard to their properties: wetting critical surface tension, expanding hole diameter, orifice coefficients, flexibility, critical and elastic pressures. The bubble formation phenomenon in an inviscid liquid at rest is studied experimentally for different membranes and gas flow rates. The variation in the bubble diameter, the bubble centre of gravity and the bubble spread on the membrane are determined as a function of time. An analytic model is proposed to describe the bubble growth and its detachment at a flexible orifice. This theoretical approach, developed by Teresaka & Tsuge (1990) for rigid orifices, is adapted to take into account the membrane features (elastic behaviour and wettability). The predicted bubble diameters at detachment agree with the experimental measurements; however, the model underestimates slightly the bubble formation times. The calculation of the various forces acting on the bubble in the vertical direction indicates that the real forces governing the bubble growth are the buoyancy force, the surface tension force, and near detachment the inertial force.

Keywords : Waste water treatment industry; Aeration; Flexible membrane sparger; Bubble formation; Image acquisition and treatment; Non spherical model.

* Corresponding author. Tel.:00 33 05 61 55 97 89; Fax:00 33 05 61 55 97 60; E-mail address: hebrard@insa-tlse.fr

1. Introduction

The aeration of a liquid with air or other gases occurs in a large number of chemical processes (oxidation, absorption, waste water treatment…). The gas, distributed by aeration systems, is released in the form of small bubbles to yield a large surface for mass transfer. In addition to the mass transfer quality, it is very important to inject and distribute the gas efficiently, that is to say, with low pressure drop and hence energy saving. In chemical industries, the aeration of liquids is mainly performed with rigid nozzles (perforated plate or porous disk diffuser) as they are able to withstand high temperatures and pressures. For waste water treatment, carried out under atmospheric conditions, a novel gas sparger based on flexible membranes was developed. This rubber punctured sheet has been reported to produce very uniform size distribution of small bubbles which leads to large increases in gas hold-up and mass transfer area (Rice & Tupperainen, 1981). Moreover, it is found to be self-cleaning and does not suffer the usual clogging problems when aeration is stopped in the tank (anaerobic period). However, these membranes are not well characterised with regard to their elastic properties, which are responsible for the advantages previously described; only a limited number of studies (Rice & Lakhani, 1983; Rice & Howell, 1986; Bischof & Sommerfeld, 1991) have been carried out on this aspect. Even though a lot of research have been performed on the behaviour in the reactor of bubbles generated from a membrane sparger, few authors have concentrated on the bubble formation and its detachment from the flexible membrane orifice. By contrast, the bubble formation at a fixed orifice has been the subject of many experimental and theoretical studies. Two detailed reviews of the literature up to 1986 and up to 1997 are respectively given by Tsuge (1986) and Sadhal et al. (1997).

The objective of the present study is to focus on the bubble formation generated from a flexible orifice in order to understand better what parameters govern the bubble size at its detachment from the orifice. For this purpose, it is first necessary to characterise the

membrane spargers: these industrial membranes are defined in terms of wetting critical surface tension, expanding hole diameter, orifice coefficients, deflection and flexibility, critical pressure and “elastic” pressure. Secondly, an experimental data bank is compiled: the bubble formation phenomenon in an inviscid liquid at rest is studied for different membranes and for different gas flow rates. Working from these two data sources, an analytic model is proposed to describe the bubble growth and detachment at a flexible orifice. The predicted bubble diameters and bubble frequencies are compared to the experimental data.

2. Theoretical model

Terasaka & Tsuge (1990), Yoo et al. (1998), Li (1999) have proposed an analytic model to describe the dynamics of the bubble growth process generated from a fixed orifice. The main points are the following: a non spherical bubble formation is considered and no empirical detachment condition is required. The objective of the present work is to make this theoretical approach suitable for predicting the bubble growth generated from a flexible orifice (membrane sparger orifice).

The modelling of bubble formation is based on the following main assumptions: the bubble grows axisymmetrically about the vertical axis on the orifice centre (2D geometry); the liquid around the bubble is incompressible, is at rest (no wake effects) and of infinite extent; the effects of the side walls and of the free surface are negligible; the gas flow is adiabatic; the gas pressures inside the bubble and in the chamber are both assumed uniform within their respective volumes.

When the increase in the pressure in the gas chamber balances the sum of resistances due to hydrostatic pressure, surface tension and, in the case of the membrane, “elastic” pressure, gas flows across the orifice and a bubble begins its growth procedure. The bubble surface moves as a result of pressure difference between the inside and the outside of the bubble. The bubble

rises during bubble growth, and the neck is formed in the final period. The bubble detaches itself when the bubble neck is closed.

2.1 Equivalent radii

The bubble surface is divided into a number N of one-dimensional axisymmetric elements which are characterised by two principal radii of curvature R and R' shown in Fig.1. R' is the radius of the circle which has the centre O and passes through the elements i-1, i and i+1, and the other radius R is the distance from the bubble's symmetrical axis to the element i through the point O. Pinczewski (1980) used the equivalent radius $\overline{R}$ defined by Eq. (1) as the characteristic radius for any point on the bubble surface:

$$\frac{1}{\overline{R}} = \frac{1}{2}\left(\frac{1}{R} + \frac{1}{R'}\right) \tag{1}$$

If a sufficient number of points is chosen to adequately represent the topology of the bubble surface then the trajectories of these points describe the movement of the gas-liquid interface.

2.2 Pressure balance on gas-liquid interface

This motion equation describes the radial expansion of the bubble. The conservation of momentum for liquid around a spherical bubble in the radial direction (axisymmetric geometry) is applied and coupled with the continuity equation for the purely extensional, incompressible and irrotational flow. The continuities of the normal stress vector and of the velocity at the interface are considered as boundary conditions. The effect of gas momentum is neglected. It leads to the modified Rayleigh equation given by Eq. (2):

$$p_B - p_h = \rho_L\left[R\frac{d^2R}{dt^2} + \frac{3}{2}\left(\frac{dR}{dt}\right)^2\right] + \frac{2\sigma_L}{\overline{R}} + \frac{4\mu_L}{R}\frac{dR}{dt} \tag{2}$$

The three terms on the right-hand side of Eq. (2) represent inertial, surface tension and viscous forces respectively. This equation is assumed to be valid for any point i on a non spherical bubble interface by replacing the global spherical radius R with the local radius of curvature R_i.

2.3 Motion equation of the rising bubble

The motion equation governing the vertical bubble ascension is described by a balance of several forces: inertial, buoyancy and viscous drag forces, the vertical component of surface tension force as well as gas momentum rate through the orifice. This force balance, applied at the bubble centre of gravity, is expressed by Eq. (3):

$$\left(\rho_G + C_I.\rho_L\right)\frac{d}{dt}(V_B.U_B) = (\rho_L - \rho_G).g.V_B - \frac{\pi D_{max}^2}{8}.C_D.\rho_L.U_B^2 - \pi.d_W.\sigma_L.\sin\theta_a + \frac{4\rho_G.q^2}{\pi.d_{OR}^2} \quad (3)$$

C_I is the added mass coefficient. Generally, the authors (Davidson & Schüler, 1960; Terasaka & Tsuge, 1990; Li, 1999) take the C_I value of 11/16 which is based on the hydrodynamics of a sphere moving perpendicularly to the wall in an inviscid fluid (Milne-Thomson, 1955). However, Marmur & Rubin (1976) use an empirical value of 0.85 to take into account the expansion motion of the bubble. The choice of 11/16 is certainly not ideal for a non spherical growing bubble in contact with a wall, but no precise information concerning this particular case is available in the literature, so it was left unchanged.

The bubble rise velocity U_B is here equal to dy/dt (vertical velocity of the bubble centre of gravity). C_D is the drag coefficient; for each operating condition, an average C_D on the bubble formation time is deduced from experimental measurements of vertical velocity and bubble diameter, by the Schiller correlation expressed as Eq. (4) and (5):

$$C_D = \frac{24}{Re_B}(1 + 0.15.Re_B^{0.687}).\alpha_L^{-1.7} \qquad Re_B<1000 \quad (4)$$

$$C_D = 0.44 \qquad Re_B>1000 \quad (5)$$

The force balance described here takes into account the special nature of membranes (i.e. their hydrophobic surface and their elastic behaviour) insofar as:

- Including the surface tension force, the orifice wettability is considered through the real surface/bubble contact diameter d_W and the contact angle θ_a (Fig.1). In the present model, d_W and θ_a are assumed to be constant during the bubble growth and deduced from experimental measurements.

- The expansion of the membrane orifice as the gas flow rate (Fig. 3) is considered in the model.

2.4 Pressure change in the gas chamber

The thermodynamic system is defined as the sum of the gas in the bubble, in the chamber and the gas that enters the chamber during the time interval dt. Assuming a polytropic behaviour of gas in the gas chamber and no pressure drop at the level of gas supply, the mass conservation equation is expressed as Eq. (6):

$$\frac{dp_C}{dt} = \frac{\chi p_C}{V_C}(Q_G - q) = \frac{\chi p_C}{V_C}(Q_G - \frac{dV_B}{dt}) \qquad (6)$$

The gas chamber volume V_C is measured experimentally. In the known literature, the polytropic coefficient χ is defined between 1 for isothermal change (Terasaka & Tsuge, 1990), and 1.4 for adiabatic change (Mc Cann et al., 1971; Li, 1999). Even though the thermodynamic behaviour of the membrane gas chamber is not usual, the polytropic coefficient is assumed to be equal to 1.4.

2.5 Orifice equation

The pressure in the bubble is related to the pressure in the gas chamber by the orifice equation as follows:

$$|p_C - p_B| = \left(\frac{q}{k_{OR}}\right)^2 = \frac{1}{k_{OR}^2}\left(\frac{dV_B}{dt}\right)^2 \qquad (7)$$

The pressure drop of the gas through the orifice results from the contracting section and from the membrane elastic properties, and is characterised by the orifice coefficient k_{OR}. Generally, the authors use empirical correlations to estimate k_{OR} in the case of rigid orifices. For flexible

orifices, no specific correlation exists, and the k_{OR} values used for rigid orifices are not appropriate because of the membrane elasticity. So, to take into account this membrane feature, the orifice coefficients included in the model are the experimental ones (Fig.6).

2.6 Initial and boundary conditions

- Initial conditions

The bubble is initially assumed to be a hemisphere with radius equal to the real surface/bubble contact surface diameter d_W (which may or may not be equal to $d_{OR,}$ depending on the membrane wettabilitity) in static equilibrium with the surrounding liquid. The reality is somewhat more complex, as the liquid flow field is affected by the preceding bubble wake. Since these effects are difficult to determine, the actual initial conditions are generally unknown and the initial bubble shape chosen represents a compromise.

The velocities and accelerations of all elements are initially taken as zero.

The initial pressure in the gas chamber is taken as the sum of the hydrostatic pressure at the orifice, the surface tension pressure and the "elastic" pressure as:

$$p_C\big|_0 = p_{atm} + \rho_L.g.H_L + \frac{4\sigma_L}{d_W} + p_O = p_B\big|_0 \qquad (8)$$

The originality of these initial conditions is to add in Eq. (8) the "elastic" pressure p_O which is a feature of flexible orifices (membrane). This pressure is determined experimentally for each membrane (Table 2).

- Boundary conditions

The element of the bubble apex i=1 moves on the symmetrical axis of the bubble.

The element contacting the orifice edge i=N does not move, so that the velocity and acceleration of this element are usually zero ("no slip" condition).

The bubble surface does not cross the orifice plate. The velocity of a downward moving point on the bubble surface is taken as zero when its trajectory intersects the plate floor.

2.7 Numerical resolution

Eqs. (1), (2), (3), (6) and (7) coupled with the initial and boundary conditions describe the dynamics of the bubble formation process. They are solved by means of a finite-difference method (Fortran 90 program). The associated algorithm is shown in the Appendix. The numerical computation is finished when the bubble neck is closed (i.e. when any element other than the apex of the bubble touches the vertical axis): the bubble also detaches from the orifice.

In order to have an accurate representation of the bubble surface, a routine is introduced which automatically inserts or deletes points when the point spacing falls outside a specified range (the initial point spacing). Moreover, a variable time step procedure is introduced; indeed, during the initial growth period, the growth rate is small, allowing a large time step, whilst near detachment a smaller time step is necessary. The approach adopted here is to halve the time step when instabilities are detected or when the time to bubble detachment is exceeded.

Typically, a calculation begins with 5-10 surface points and finishes with 40-80 surface points.

3. Experimental set-up and methods

3.1 Experimental set-up

Fig.2 shows a schematic diagram of the experimental set-up. The experiments are carried out in a glass parallelepiped vessel (1), 0.40 m in width, 0.40 m in length, 0.30 m in height, regulated in temperature (water circulation). The flow rate of air is controlled by a pressure gauge (5) and regulated by a gas flow meter (6). The membrane sparger is assembled on a circular clamping ring (2) composed of two jaws; this fixing system coupled with the use of a dynamometric spanner (0-5 Nm) enables the same initial tension to be applied, thus giving

reproducible results whatever the membranes. The pressure drop created by the membrane is determined using an electronic manometer type BIOBLOCK 915PM247 (7). The bubbles are generated by a single puncture located at the membrane centre. The average gas flow rate is measured using a soap film meter (4) , through a funnel (3) put on the clamp. Water is used as the liquid phase; for each experiment, the water physical properties are measured and are the following: σ_L=71.8 mN/m, μ_L=8.74 .10^{-4} Pa.s, ρ_L=997 kg/m^3. The operating conditions are as follows: liquid height H_L=20 cm, gas chamber volume V_C=107-111 cm^3 (depending on the membrane bulging). The gas flow rates studied correspond to those used in industrial aeration tank (typically about 0.4-0.8 ml/s by hole).

Referring to Tsuge (1986) and Räbiger & Vogelpohl (1986), dimensionless numbers are defined to characterise the bubble formation from a fixed orifice: the dimensionless capacitance number N_C (gas injection condition), the dimensionless gas flow rate N_W (bubbling regimes) and the Weber number We (transition to the jetting regime). They are mentioned in Table 1 for the operating conditions studied. Even though the bubble generation system used is not usual (flexible orifice), all the N_C values are well above 9, which corresponds to the constant-pressure condition (i. e. there is no fluctuation of the pressure in the gas chamber). The N_W values are below 16: the bubbling regime is also dynamic; the jetting regime is not reached (low We numbers).

3.2 Membrane spargers

Four different types of industrial rubber membrane spargers are studied: M1, M2, M3 and M4, which have a diameter of 60 mm. Punctures were distributed over all the surface sheet. Consequently, it was necessary to close all the holes except for the central one, without modifying the elastic membrane properties: a silicone elastomer glue applied on the inner surface (gas chamber side) was used.

In Table 2, the membranes thickness and their wettability property are given. The wetting critical surface tension of the membranes γ_C describes the membrane surface property and is determined experimentally by the method developed by Fox & Zisman (1952). γ_C is very low (very similar to that of silicone material): the membrane surfaces are clearly hydrophobic, especially for the M4 membrane.

3.3 Image acquisition and treatment systems

During their formation, the bubbles are photographed with a Leutron LV95 camera (360 images/s). Images are visualised on the acquisition computer through the Leutron vision software. The measurements of membrane deflections at the centreline are also performed by this acquisition system. Without liquid phase, the hole diameter measurements are based on the joint use of a Sony DXC 930P 3CCD Colour camera and a Nikon SMZ-U microscope. The image treatment is performed with the Visilog 5.2 software. It consists of a thresholding, followed by different arithmetical and geometrical operators (C^{++} program). As a result, the following parameters are determined: equivalent bubble (or hole) diameter, centre of gravity co-ordinates, shape factor, contact angles and neck diameter. The bubble frequency is deduced from photographic analysis. The experimental errors on the bubble diameter, hole diameter and neck diameter measurements are respectively 10 %, 12 % and 15 %.

4. Results and discussion

4.1 Membrane sparger characterisation

- Equivalent hole diameter.

The dynamic rubber membrane behaviour was studied experimentally. Using the image acquisition system previously described, hole diameters are measured. They correspond to the equivalent diameters defined from the area assuming a circular hole, given by Eq. (9):

$$d_{OR} = \left[\frac{4.(\text{Hole Area})}{\pi} \right]^{1/2} \quad (9)$$

These equivalent hole diameters are calculated from an area which is determined from the image considered; so, it is difficult to say with certainty that this measured area is the same through the entire membrane thickness and that the equivalent diameter is the effective one. Nevertheless, Fig.3 shows that, for all membranes, the apparent equivalent hole diameter increases with an increase in gas flow rate: this dependence of the orifice diameter with the gas flow rate is a major difference with regard to a rigid orifice. It can be explained by the fact that, when the pressure increases, the hole expands owing to its elastic nature. Moreover, the orifice size varies in shape: at low expansions (small applied pressures), the puncture appears as a slit and as the pressure increases, the slit expands to form a more circular shape (cf. photographs in Fig.4). The largest and the smallest hole diameters are obtained respectively with the M1 and M4 membranes.

- Relation between applied pressure drop and gas flow rate; Orifice coefficients.

The experimental curves relating the applied pressure drop and the gas flow rate through the hole are presented in Fig.5 for the four membranes. It is noted there is a hysteresis when comparing the flow as pressure increases to the flow as pressure decreases. This is more severe with the M1 membrane. This phenomenon is observed for all the measurements (hole diameter, deflection..). All the results presented were obtained as pressure decreases. Moreover, Fig.5 highlights some different membrane behaviours in terms of pressure drop; for a given gas flow rate, the applied pressure for the M1 membrane is four times greater than the three other membranes. The M2 membrane needs the lowest applied pressure. This experimental observation has important consequences in terms of energy consumption in a waste water treatment plant.

The data of Fig.5 are translated into dimensionless numbers: the discharge factor f and the Reynolds number Re for gas through the orifice. The relation between f and Re is expressed as Eq. (10):

$$f = \alpha.Re^{\beta} = \frac{\Delta p}{\frac{1}{2}.\rho_G.U_G^2} \quad (10)$$

The α and β values for the four membranes are presented in Table 2 (Re: 5-1000). By combining the expression of discharge factor (Eq. (10)) and the orifice equation (Eq. (7)), the experimental orifice coefficient can be deduced as Eq. (11):

$$k_{OR} = \frac{\pi.d_{OR}^2}{\sqrt{8.f.\rho_G}} \quad (11)$$

$|p_C-p_B|$ is assumed to be equal to the applied pressure measured experimentally. The experimental orifice coefficients as a function of hole diameter are shown in Fig.6. It can be noted that orifice coefficients increase with an increase in hole diameter and a decrease in discharge factor. The greatest discharge factors are obtained for the membrane M1.

The orifice coefficient characterises the pressure drop of the gas through the orifice. Low values of k_{OR} are linked to high discharge factors, so to large pressure drops. Compared to a rigid orifice, the orifice coefficients are widely lower with membranes, resulting from the membrane elasticity.

- Deflection and flexibility

As increasing pressure is applied, it causes the membrane to bulge: the membrane takes on thus the shape of a spherical cap. Using the acquisition system, membrane deflections at the pole are measured experimentally for each applied pressure ΔP. The curves relating deflection W_O versus pressure drop are shown in Fig.7. It can be observed that the deflection at the pole increases with pressure for all membranes. The largest and the smallest deflections are obtained with the membranes M4 and M3 respectively. Rice & Lakhani (1983) have

developed a theory to show the connection between elastic and flow mechanics in order to describe the membrane behaviour when subjected to pressure from below. They show that excess tension T can be related to applied pressure by Eq. (12):

$$T = K.\Delta P^{n} \tag{12}$$

where T is a function of applied pressure, deflection, membrane radius; K and n are characteristic properties of the membrane determined experimentally. K and n values for the four membranes are shown in Table 2. Large values of K are associated with small deflections. For the M3 membrane, K is equal to 1.84 whereas K is about 0.20 for the others. This result agrees with deflection measurements (Fig.7). In view of these results, it appears that the M3 membrane has the lowest flexibility.

- Critical pressure and “elastic” pressure

Rice & Howell (1986) and Bischof & Sommerfeld (1991) have proposed the force balance described in Fig.8 for a bubble formed at a flexible nozzle. In contrast to a rigid nozzle, the force due to the elasticity of the material has also to be taken into consideration. The required pressure which allows the formation of a bubble is given by Eq. (13):

$$\Delta p > p_C - p_H + p_{HB} - p_\sigma - p_O \tag{13}$$

where the capillary pressure p_σ is equal to $4\sigma/d_{OR}$, assuming no bubble spreading on the membrane. The hydrostatic correction for bubble height ($p_{HB} = \rho.g.r_B$) is negligible. The “elastic” pressure p_O which depends on the properties of the flexible membrane is unknown and has to be determined experimentally. The present authors decided to define the critical pressure Δp_C to just initiate bubbling as Eq.(14):

$$\Delta p_C = \frac{4\sigma_L}{d_{OR}} + p_O \tag{14}$$

The critical pressure is essentially a measured quantity, determined as the lowest pressure necessary to induce the formation of the first bubble. These Δp_C values for the membranes are

shown in Table 2. The highest and the lowest critical pressures are obtained for the M1 and M2 membranes respectively: this observation agrees with the $Q_G=f(\Delta P)$ results in Fig.4. Hence, it is possible to deduce the "elastic" pressure p_O from Eq. (14) with measured critical pressure and associated hole diameter. The experimental p_O values are expressed in Table 2. The same conclusions as for the critical pressures are observed.

4.2 Study of the bubble formation generated from a flexible orifice

- Dynamics of the bubble formation

Fig.9 (a) and (b) show typical photographs of bubble formation generated from the M2 and M1 membranes (respectively Q_G=0.09 ml/s and 0.03 ml/s). Thanks to image treatment, the bubble formation process is described experimentally, from bubble birth to its detachment. Fig.10 illustrates an example of the centre of gravity curves versus growing time (M1 membrane Q_G=0.03 ml/s). The centre of gravity abscissa is nearly nil during formation time: the bubble symmetry about the vertical orifice axis is proven. A good agreement between the centre of gravity ordinate and the bubble radius is obtained, thus the bubble growth is spherical. As shown in Fig.10, two stages appear during the formation : the "expansion stage" where $y<R_B$ (radial expansion) and the "detachment" stage where $y>R_B$ (bubble elongation, neck formation). These stages in bubble formation correspond to those of Ramakrishnan & Kumar (1969).

Fig.11 shows a typical trace of the bubble vertical velocity versus formation time (M1 membrane). At the beginning of the bubble formation, the vertical velocity (dy/dt) decreases until it reaches an almost constant velocity; afterwards, the velocity increases continuously until the bubble detaches. Such a behaviour can be confirmed by the vertical acceleration trace shown in Fig.12 (M1 membrane): at first, the acceleration (d^2y/dt^2) is negative (deceleration) and becomes nearly nil; then, the bubble begins to accelerate until its detachment. Moreover, an increasing gas flow rate tends to increase the vertical velocity and

acceleration (Fig.11 and Fig.12). The profiles of centre of gravity, vertical velocity and acceleration presented in Fig.10, Fig.11 and Fig.12 are observed whatever the gas flow rates and whatever the membranes, except for the M4 membrane. In fact, the orifice of this membrane is perforated not vertically with regard to the thickness, but slantwise. As a result, the bubbles generated are not perfectly symmetrical about the vertical orifice axis.

- Bubble adhering to membrane surface

As mentioned previously, membrane surfaces are clearly hydrophobic. This observation has consequences for the contact between the gas bubble and the membrane surface. In order to highlight this phenomenon, two parameters are chosen and determined experimentally: the surface/bubble contact diameter d_W and the contact angles θ_a and θ_r. The ratio d_W/d_{OR} as a function of formation time is plotted in Fig.13 for different gas flow rates (M4 membrane). Whatever the gas flow rate, this ratio is clearly higher than 1: gas bubbles spread over the membrane surface; the line of contact between the bubble and the solid doesn't correspond to the orifice perimeter. An increasing gas flow rate tends to intensify this phenomenon. It has important consequences on the bubble formation time and on the detached bubble diameter. When the membrane nature is hydrophobic, the surface tension force applied on the bubble is increased, which tends to keep the bubble attached to the orifice: the bubble formation process is also slower, generating larger bubbles. So, to produce smaller bubbles, a membrane surface treatment is necessary: a higher wetting critical surface tension should be obtained to limit the bubble spread on the membrane.

Fig.14 shows the typical variation of the two bubble contact angles, θ_a and θ_r, during the bubble growth (M3 membrane; Q_G=0.03 ml/s). There is no difference between the two contact angles, which confirms the symmetrical formation of the bubble. It can be noted that the contact angle decreases with the formation time. No significant effect of gas flow rate is observed on the contact angles.

Fig.15 compares the curves for the ratios d_W/d_{OR} for the four membranes (Q_G=0.26 ml/s). The bubble spreading phenomenon is the most pronounced for the M4 membrane: this observation agrees with the wetting critical surface tension (Table 2).

- Bubble diameter and bubble frequency

Fig.16 shows the relation between bubble diameter and gas flow rate for the four membranes. At first, it can be noted that bubble diameter increases logarithmically with gas flow rate. Such a behaviour is specific to membrane spargers : an inverse behaviour is observed for bubbles generated from perforated plate spargers (Hebrard et al., 1996). The bubble diameter trace presented in Fig.16 is caused by the fact that with higher gas flow rates, the pressure below the membrane increases and yields a larger hole in the material when it bulges. Hebrard et al. (1996) and Couvert et al. (1999) have obtained similar profiles of d_B versus Q_G in bubble columns and in an air-lift reactor equipped with membrane spargers respectively. These observations would indicate that the size of the bubbles generated by the membrane is determined at the moment of detachment and appears to be maintained afterwards in the reactor. It is likely the small size of these bubbles which renders them stable to coalescence and breaking phenomena. It becomes also very important to be able to predict the bubble diameter generated from a flexible membrane orifice.

Comparing the four membranes, the largest bubbles are produced with the M1, whatever the gas flow rate. The differences between membranes are more pronounced with low Q_G (below 0.5 ml/s) than for high Q_G (above 0.5-0.8 ml/s): generally, the M2, M3 and M4 membranes generate bubbles of comparable sizes (about 10-20 % difference).

The bubble frequency curves as a function of gas flow rate are given in Fig.17 for all membranes. The lowest and the highest bubble frequencies are found for the M2 and the M1 membranes respectively, but differences in behaviour are also observed. For the M1 membrane, bubble frequency clearly increases with an increase in Q_G whereas for all the other

membranes, the bubble frequency reaches a constant value above a critical gas flow rate. For any given bubble diameter, the different bubble frequencies obtained for the four membranes should involve different gas hold-up and mass transfer coefficients.

- Comparison between experimental and calculated bubble growth curves

Firstly, the resolution of the equations system presented previously is tested for bubbles generated from fixed orifices. Table 3 shows a comparison of experimental data of Terasaka & Tsuge (1990) with results calculated by the present model. These authors studied the bubble formation generated from a fixed orifice in distilled water and in a highly viscous liquid (glycerol) for different gas chamber volumes. The initial time step is 50 μs. The initial surface point number varies between 4 and 15, depending on the case. At detachment, an average of 80 points describes the bubble surface. As shown in Table 3, a good agreement is observed between the experimental and the computed bubble diameters and bubble formation times. The differences are below 15 %, which corresponds to the experimental error. Our numerical resolution is also validated.

As shown in §2, the model has been adapted to predict the bubble formation generated from a flexible orifice. The membrane features (i.e. elastic behaviour and wettability) are taken into account through several parameters: the orifice coefficient k_{OR}, the elastic pressure p_O, the expanding hole diameter d_{OR}, the surface/bubble contact diameter d_w and the contact angle θ_a.

An example of the theoretical bubble shape variation with time is shown in Fig.18 (Membrane M3 Q_G=0.49 ml/s). Obviously, the change in shape predicted by the present model proves that the bubble detachment is a natural consequence of the dynamics of the bubble formation process. Furthermore, this development in spherical shape and the neck formation agree with the experimental observations made by the camera visualisation and image analysis.

Typical traces of the bubble volume versus formation time are plotted in Fig.19. A quite good agreement is observed between the experimental and calculated bubble volume. It can be noticed that at the beginning of the bubble growth (radial expansion stage), the model tends to underestimate the bubble volume.

Comparisons of the detached bubble diameter and of the bubble formation time are presented in Fig.20 and Fig.21 respectively between the experimental measurements and the numerical results, under different operating conditions (two gas flow rates per membrane). For all the simulations, the initial time step is 5 μs and the initial surface point number is 5. At detachment, about 50 to 100 points describe the bubble surface. The predicted and the measured bubble diameters are in good agreement: the difference is below 15%. However, the model underestimates the bubble formation time in most cases: an average difference of 30% is observed. This is especially true for low gas flow rates (Q_G<0.5 ml/s).

Two hypotheses can be put forward to explain this result. Firstly, the model resolution is very sensitive to orifice coefficient and initial elastic pressure applied. It can be observed that the experimental orifice coefficients are generally underestimated; to have accurate results, a corrective factor is applied to the experimental k_{OR} and varies between 1,5 and 7 for high gas flow rates (above 0.5 ml/s) and between 7 and 15 for low gas flow rates. Moreover, the experimental p_O values are too high, which provokes a premature detachment. In most cases, the elastic pressure imposed in initial condition (Eq.8) should be below 50 Pa in order to obtain accurate formation time values. These two remarks prove that k_{OR} and p_O are two key parameters and at present, they are not well managed. The second hypothesis to explain these calculated formation times concerns the triple point i=N where the bubble, the liquid phase and the membrane surface are in contact. The present model assumes that this point does not move during the bubble growth; its abscissa is taken as the surface/bubble contact diameter d_W divided by two. Experimentally, it has been shown that the bubble spread on the

membrane surface varies with the growth time (Fig.13 and Fig.15). In the future, a slip condition on the triple point has to be included to take into account this experimental observation.

Typical variations in the calculated pressures in the gas chamber p_C and in the bubble p_B during the bubble growth are plotted in Fig.22 (Membrane M3 Q_G=1.10 ml/s). The pressure in the bubble decreases slightly as a function of the formation time. The pressure in the gas chamber is nearly constant whatever the formation time. This last observation agrees with the calculated values of the capacitance number N_C (Table 1); indeed, the operating conditions lead to N_C values above 9, corresponding to the constant-pressure condition. Moreover, some experimental measurements of the pressure in the gas chamber were performed using a piezoresistive pressure transmitter (sensitivity of 1mbar): no pressure variation was observed under the membrane orifice.

To understand the dynamics of the bubble growth, the various forces acting on the bubble in the vertical direction are calculated using experimental data (the co-ordinates of bubble centre of gravity and the associated velocities and accelerations, the bubble volume and the surface/bubble contact diameter variations in the growth time). These forces are expressed as follows:

- the buoyancy force F_B:

$$F_B = (\rho_L - \rho_G).g.V_B \tag{15}$$

- the force related to the gas momentum through the orifice F_m:

$$F_m = \frac{4.\rho_G.(\frac{dV_B}{dt})^2}{\pi d_{OR}^2} \tag{16}$$

- the surface tension force F_S:

$$F_S = -\pi d_W.\sigma_L.\sin(\theta_a) \tag{17}$$

- the viscous drag force F_D:

$$F_T = -\frac{1}{2}.\rho_L.(\frac{\pi d_B^2}{4}).C_D.(\frac{dy}{dt})^2 \quad (18)$$

- the inertial (or added mass) force F_I:

$$F_I = -(\rho_G + \frac{11}{16}\rho_L)\left[\frac{dy}{dt}.\frac{dV_B}{dt} + \frac{d^2y}{dt^2}.V_B\right] \quad (19)$$

The force values deduced from experimental data are compared with the forces predicted by the present model. This comparison is shown in Fig.23 for the membrane M3 (Q_G=1.10 ml/s). A quite good agreement is observed between the "experimental" and the "numerical" forces, even though the model tends to underestimate the forces. Concerning the surface tension force, the difference is caused by the fact that a constant surface/bubble contact diameter is considered in the model whereas the experimental d_W varies with the formation time (Fig.13 and Fig.15). Nevertheless, some interesting conclusions can be drawn. The drag and the gas momentum forces are negligible throughout the bubble growth. The inertial force is small during the initial growth period, whilst near detachment it becomes more important (about 10^{-5} N), resulting from the final bubble acceleration (Fig.12). The real forces governing the bubble growth are, on the one hand, the buoyancy force (about 10^{-5}-10^{-4} N) which tends to detach the bubble and, on the other hand, the surface tension force (about 10^{-4} N) which keeps the bubble attached to the orifice. This last observation confirms the importance of the membrane wettability.

5. Conclusion

The bubble formation in an inviscid liquid at rest has been investigated for different flexible orifices (industrial membrane spargers) and gas flow rates. The following conclusions can been drawn from this work:

- Concerning the membrane characterisation, it has been shown that the membrane surface is clearly hydrophobic. The dynamic membrane behaviour has been proven

(expanding hole and membrane bulging). The orifice coefficients k_{OR} have been determined: compared to rigid orifices, they are widely lower. The critical and the elastic pressures have been measured for each membrane.

- The bubble formation mechanism has been studied experimentally by measuring the bubble diameters and the variation in its centre of gravity position during bubble growth. These findings confirm the bubble symmetry about the vertical axis and the existence of two phases in the bubble growth.
- The phenomenon of the bubble spread on the membrane surface has been demonstrated: an increasing gas flow rate intensifies this phenomenon.
- The variation in the bubble diameter at detachment as a function of gas flow rate is logarithmic, as Hebrard et al. (1996) had obtained within bubble columns equipped with membrane spargers. This result would indicate that small bubbles generated by the membrane remain stable in the face of coalescence or breaking phenomena.
- The industrial membranes produce bubbles of comparable sizes. Nevertheless, significant differences in the bubble frequencies between membranes are observed, involving different gas hold-up.
- A non spherical bubble formation model at a flexible orifice has been proposed: developed by Teresaka & Tsuge (1990) for rigid orifices, this model has been adapted to take into account the membranes features (elastic behaviour and wettability). The predicted bubble diameters at detachment agree with the experimental measurements; however, the predicted bubble formation times are widely underestimated. Even though the calculations are globally acceptable, this model has to be improved: the orifice coefficient, the elastic pressure and the surface tension force appear to be key parameters and at present, they are not well managed.

- The calculation of the various forces acting on the bubble in the vertical direction indicates that the drag and the gas momentum forces are negligible during the bubble growth; for the bubbles generated from a flexible orifice, the real forces governing the bubble growth are the buoyancy force, the surface tension force and near detachment the inertial force.

Notation

a	membrane radius	[m]
C_D	drag coefficient	[-]
C_I	added mass coefficient	[-]
d_B	bubble diameter	[m]
D_{max}	maximum horizontal bubble diameter	[m]
d_{OR}	equivalent hole diameter	[m]
d_W	surface/bubble contact diameter	[m]
dy/dt	vertical velocity of the bubble centre of gravity	[m/s]
d^2y/dt^2	vertical acceleration of the bubble centre of gravity	[m^2/s]
f_B	bubble frequency	[s^{-1}]
F_B	buoyancy force	[N]
F_D	viscous drag force	[N]
F_I	inertial (or added mass) force	[N]
F_m	force related to the gas momentum through the orifice	[N]
F_s	surface tension force	[N]
g	gravity acceleration	[m/s^2]
H_L	liquid height	[m]
K	constant from Eq. (12)	[-]
k_{OR}	orifice coefficient	[$m^{7/2}/kg^{1/2}$]
n	constant from Eq. (12)	[-]
N	surface element number	[-]
p_{atm}	atmospheric pressure	[Pa]
p_B	pressure inside the bubble	[Pa]
p_C	pressure in the gas chamber	[Pa]
p_h	hydrostatic pressure at the element i	[Pa]

p_H	hydrostatic pressure ($p_{atm} + \rho_L.g.H_L$)	[Pa]
p_{HB}	hydrostatic pressure for bubble height ($\rho_L.g.R_B$)	[Pa]
p_σ	pressure due to surface tension (capillary)	[Pa]
p_O	pressure due to membrane elasticity	[Pa]
Δp	applied pressure drop	[Pa]
Δp_C	critical pressure	[Pa]
q	gas flow rate through the orifice ($q=dV_B/dt$)	[m^3/s]
Q_G	gas flow rate	[m^3/s]
R	bubble radius of curvature defined in Eq. (1)	[m]
R’	bubble radius of curvature defined in Eq. (1)	[m]
$\overline{R}$	equivalent bubble radius from Eq. (1)	[m]
R_B	bubble radius	[m]
T	excess tension $T = \Delta p.a^2/4W_O + \Delta p.W_O/4$	[Pa.m]
t_B	bubble formation time	[s]
U_B	bubble rise velocity	[m/s]
U_G	gas velocity through the orifice	[m/s]
V_C	gas chamber volume between the control valve and the orifice	[m^3]
V_B	bubble volume	[m^3]
x	abscissa of the bubble centre of gravity	[m]
y	ordinate of the bubble centre of gravity	[m]
W_O	membrane deflection at the pole	[m]

Dimensionless numbers

f	discharge factor defined by $f = \Delta p/(1/2.\rho_G.U_G^2)$	[-]
Bo	Bond number defined by $Bo = \rho_L.d_{OR}^2.g/\sigma_L$	[-]
Fr	Froude number defined by $Fr = U_G^2/(d_{OR}.g)$	[-]
N_C	capacitance number defined by $N_C = 4V_C.\rho_L.g/(\pi d_{OR}^2 p_H)$	[-]
N_W	gas flow rate number defined by $N_W = Bo.Fr^{0,5}$	[-]
Re	hole Reynolds number defined by $Re = U_G.\rho_G.d_{OR}/\mu_G$	[-]
Re_B	bubble Reynolds number defined by $Re_B = U_B.\rho_L.d_B/\mu_L$	[-]
We	Weber number defined by $We = U_G^2.d_{OR}.\rho_G/\sigma_L$	[-]

Greek symbols

α	constant from Eq. (10)	[-]

α_L	liquid hold-up (1 in our case)	[-]
β	constant from Eq. (10)	[-]
γ_C	wetting critical surface tension of the membrane surface	[N/m]
μ_G	gas viscosity	[Pa.s]
μ_L	liquid viscosity	[Pa.s]
ρ_G	gas density	[kg/m^3]
ρ_L	liquid density	[kg/m^3]
σ_L	liquid surface tension	[N/m]
θ_a, θ_r	bubble contact angles	[°]
χ	polytropic coefficient	[-]

Acknowledgements

The authors gratefully acknowledge the help of the students from the Mathematics & Modelling Department of I.N.S.A. in the model programming: many thanks to Nolwenn Balin, Caroline Bidot, Davy Lan Nang Fan et Aurélie Pierrache. The authors extend their sincere thanks to Zdravka Do-Quang and the ONDEO for their financial support.

Appendix

To solve the non spherical bubble formation model numerically, the following algorithm of the finite-difference procedure is used:

1) Definition of the operating conditions, of the initial time step and of the initial surface point number; Parameter initialisation.
2) Provided that the bubble does not detach (principal loop)
   (a) For each point i of the bubble surface:

- The radii $R_i\big|_{t-\Delta t}$, $R'_i\big|_{t-\Delta t}$ and $\overline{R_i}\big|_{t-\Delta t}$ are calculated geometrically (using the co-ordinates of the point i at t-Δt).

- The modified Rayleigh equation is solved by the Runge-Kutta method (order 4) giving $\left.\frac{d^2R_i}{dt^2}\right|_t$. The radial velocity and the radial displacement of each element are also:

$$\left.\frac{dR_i}{dt}\right|_t = \left.\frac{dR_i}{dt}\right|_{t-\Delta t} + \Delta t.\left.\frac{d^2R_i}{dt^2}\right|_t \qquad \text{(A-1)} \qquad\qquad \Delta R_i\big|_t = \Delta t.\left.\frac{dR_i}{dt}\right|_t \qquad \text{(A-2)}$$

(b) Calculation of the intermediary $V_B\big|_t$ (only the bubble radial expansion is considered).

(c) The force balance is solved by the Runge-Kutta method (order 4) giving $\left.\frac{d^2y}{dt^2}\right|_t$. The vertical velocity and the vertical displacement of the bubble centre of gravity are described by:

$$\left.\frac{dy}{dt}\right|_t = \left.\frac{dy}{dt}\right|_{t-\Delta t} + \Delta t.\left.\frac{d^2y}{dt^2}\right|_t \qquad \text{(A-3)} \qquad\qquad \Delta y\big|_t = \Delta t.\left.\frac{dy}{dt}\right|_t \qquad \text{(A-4)}$$

(d) Calculation of the new co-ordinates of all elements and of the new bubble volume at time t.

(e) The change in pressure in the gas chamber at time t is obtained from an integral equation:

$$p_C\big|_t = p_C\big|_{t-\Delta t}.e^{\frac{\chi.\Delta t}{V_C}.\left[Q_G - \left.\frac{dV_B}{dt}\right|_t\right]} \qquad \text{(A-5)}$$

(f) The pressure inside the bubble is:

$$p_B\big|_t = p_C\big|_t - \frac{1}{k_{OR}^2}.\left(\left.\frac{dV_B}{dt}\right|_t\right)^2 \qquad \text{(A-6)}$$

(g) Comparison of the bubble volumes calculated in the steps (b) and (d). The error is verified to be negligible.

(h) Test on the required conditions to halve the time step. If necessary, the procedure is repeated from step (a) with $\Delta t/2$.

(i) Test on the required conditions to insert or to delete surface points. Calculation of the co-ordinates of the new points.

(j) If any surface point ($i \neq 1$) touches the vertical axis (i.e. if the bubble does not detach), the procedure begins to the principal loop (2. (a)) with $t+\Delta t$ again. Else, the bubble detaches, the procedure continue on the step (3)

3) The bubble detaches. The final bubble diameter, the frequency and the variation in all parameters as a function of growth time are given.

References

Bischof F., & Sommerfeld M. (1991). Studies of the bubble formation process for optimisation of aeration systems. *Proceeding of the International Conference on Multiphase Flows,* Tsukuba, September 24-27 1991, Japan.

Couvert A., Roustan M., & Chatellier P. (1999). Two-phase hydrodynamic study for a rectangular air-lift loop reactor with an internal baffle. *Chemical Engineering Science,* 54, 21, 5245-5252.

Davidson J.F., & Schüler B. O. G. (1960). Bubble Formation at an orifice in a inviscid liquid. *Trans. Instn Chem. Engrs,* 38, 335.

Fox H.W., & Zisman W.A. (1952). *Journal Colloid Science*.,7, 428.

Hebrard G., Bastoul D., & Roustan M. (1996). Influence of the gas spargers on the hydrodynamic behaviour of bubble columns. *Trans IchemE,* 74, A, 406-414.

Li H. Z. (1999). Bubbles in non-Newtonian fluids: Formation, interactions and coalescence. *Chemical Engineering Science,* 54, 2247-2254.

Mc Cann D.J., & Prince R.G.H. (1971). Regimes of bubbling at a submerged orifice. *Chemical Engineering Science,* 26, 1505-1512.

Marmur A., & Rubin E. (1976). A theoretical model for bubble formation at an submerged orifice in an inviscid liquid. *Chemical Engineering Science,* 11, 453.

Milne-Thomson L.N. (1955). Theoretical Hydrodynamics. *London : MacMillan & Co Ltd.,* 3rd edition.

Pinczewski W. V. (1980). The formation and growth of bubbles at a submerged orifices. *Chemical Engineering Science,* 36, 405-411.

Räbiger N., & Vogelpohl A. (1986). Bubble formation and its movement in Newtonian and non Newtonian liquids. *Encyclopaedia of Fluid Mechanics (Edited by Cheremisinoff), Gulf Publishing Corporation, Houston, TX,* 43, Chap. 4, pp 58-88.

Ramakrishnan S., Kumar R., & Kuloor N.R. (1969).Studies in bubble formation – I : Bubble formation in constant flow conditions. *Chemical Engineering Science*, 24, 731-747.

Rice R.G., & Tupperainen J.M.I. (1981). *Canadian Journal of Chemical Engineering,* 59, 677.

Rice R.G., & Lakhani N.B. (1983). Bubble Formation at a puncture in a submerged rubber membrane. *Chem Eng Commun,* 24, 215-234.

Rice R.G., & Howell S.W. (1986). Elastic and flow mechanics for Membrane spargers. *AIChE Journal,* 32, 8.

Sadhal S.S., Ayyaswany P.S., & Chuang J.N. (1997). Transport Phenomena with Drops and Bubbles, *Springer Verlag,* New York.

Terasaka K., & Tsuge H. (1990). Bubble Formation at a single orifice in highly viscous liquids. *Journal of Chemical Engineering of Japan,* 23, 160-165.

Tsuge H. (1986). Hydrodynamics of bubble formation from submerged orifice. *Encyclopaedia of Fluid Mechanics (Edited by Cheremisinoff), Gulf Publishing Corporation, Houston, TX,* 43, Chap. 9, pp 191-232.

Yoo D.-H., Tsuge H., Terasaka K., & Mizutani K. (1997). Behaviour of bubble formation in suspended solution for an elevated pressure system. *Chemical Engineering Science,* 52, 21/22, 3701-3707.

Figure legend

Figure 1: Schematic diagram of non spherical bubble formation model

Figure 2: Schematic diagram of the experimental set-up

Figure 3: Equivalent hole diameter versus gas flow rate

Figure 4: Hole photographs

Figure 5 : Gas flow rate through the hole versus applied pressure

Figure 6: Experimental orifice coefficient versus hole diameter

Figure 7: Membrane deflection at the pole versus applied pressure

Figure 8: Force balance during bubble formation at a flexible nozzle

Figure 9: Bubble formation photographs

Figure 10: Bubble radius, co-ordinates of bubble centre of gravity versus formation time

Figure 11: Vertical velocity of the bubble centre of gravity versus formation time for different gas flow rates

Figure 12: Vertical acceleration of the bubble centre of gravity versus formation time for different gas flow rates

Figure 13: Ratio of surface/bubble contact diameter and hole diameter versus formation time for different gas flow rates

Figure 14: Contact angles versus formation time

Figure 15: Ratio of surface/bubble contact diameter and hole diameter versus formation time for the four membranes

Figure 16: Bubble diameter versus gas flow rate

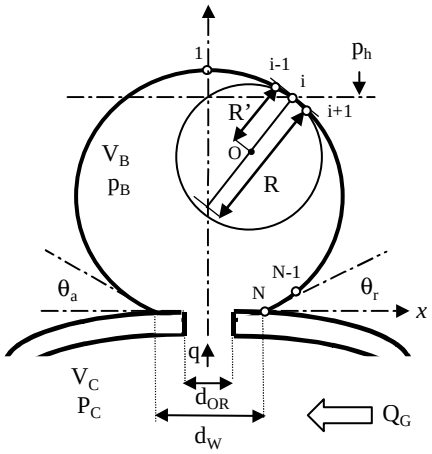

Fig.1. Schematic diagram of non spherical bubble formation model

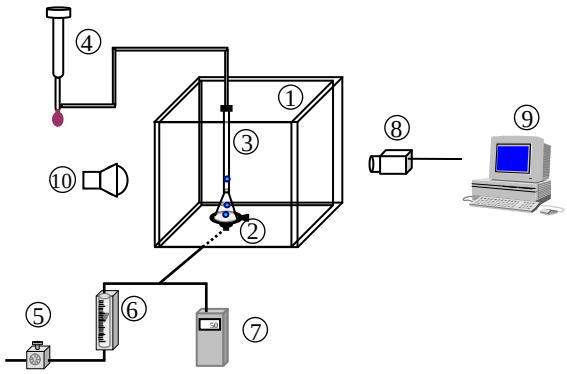

Fig.2. Schematic diagram of the experimental set-up
1: Bubble generation vessel, 2: Membrane clamp, 3: Funnel, 4: Soap film meter, 5: Pressure gauge, 6: Gas flow meter, 7: Electronic manometer, 8: Video camera, 9: Acquisition computer, 10: Halogens lamp

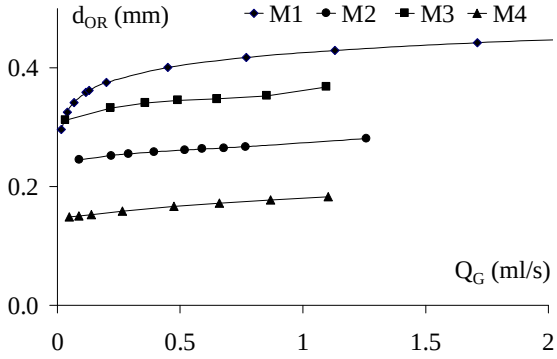

Fig.3. Equivalent hole diameter versus gas flow rate

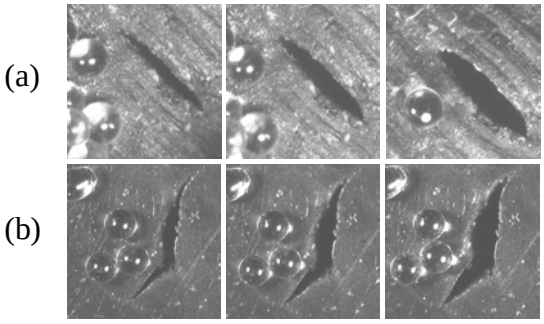

Fig.4. Hole photographs
(Calibration: glass particle 300µm in diameter) (a): M2 membrane ΔP=15, 96, 197 mbars (b) M3 membrane ΔP=21, 89, 182 mbars

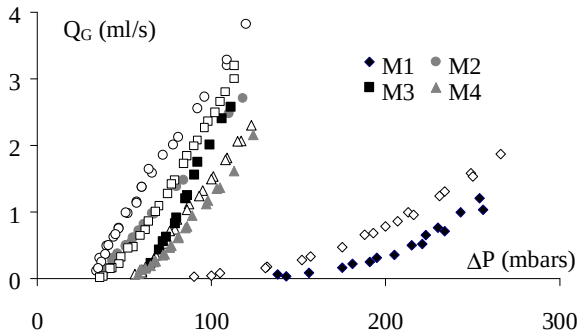

Fig.5. Gas flow rate through the hole versus applied pressure (Filled symbol: ΔP increasing; Not-filled symbol: ΔP decreasing)

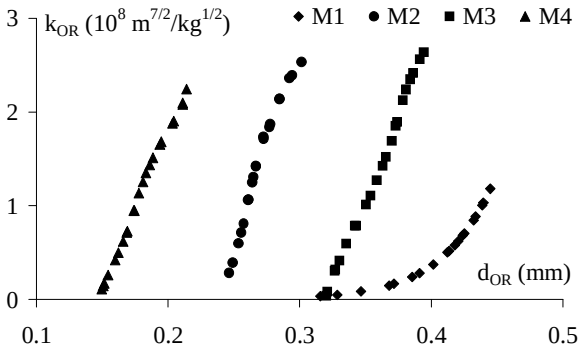

Fig.6. Experimental orifice coefficient versus hole diameter

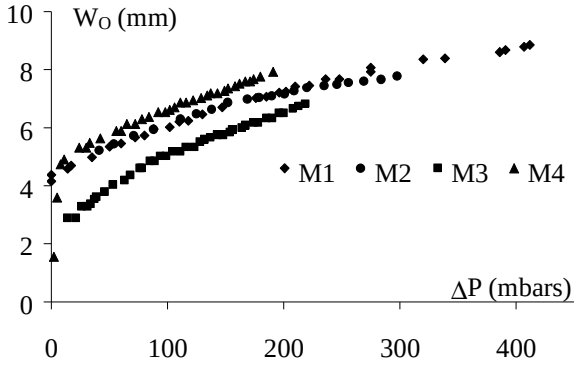

Fig.7. Membrane deflection at the pole versus applied pressure

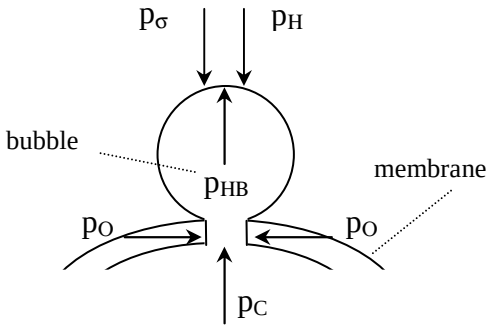

Fig.8. Force balance during bubble formation at a flexible nozzle

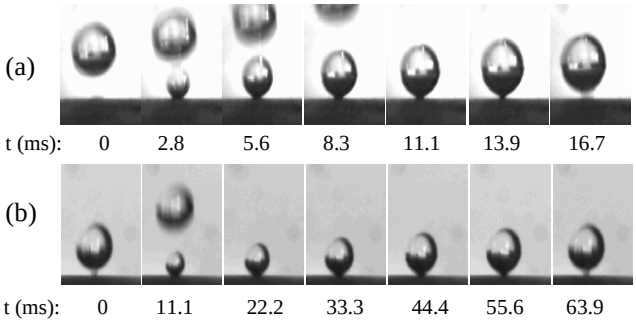

Fig.9. Bubble formation photographs
(a) M2 membrane Q_G=0.09 ml/s. (b) M1 membrane Q_G=0.03 ml/s

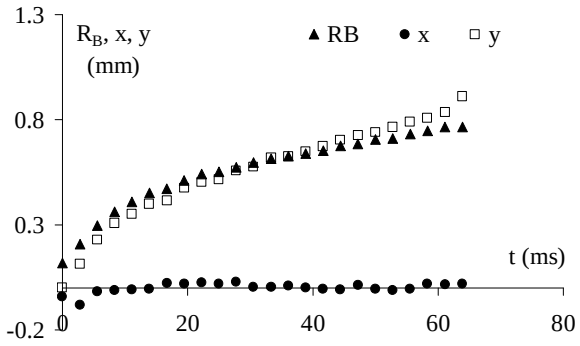

Fig.10. Bubble radius, co-ordinates of bubble centre of gravity versus formation time (M1 membrane Q_G=0.03 ml/s)

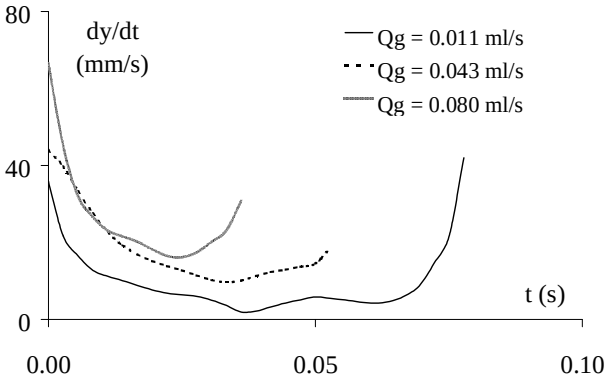

Fig.11. Vertical velocity of the bubble centre of gravity versus formation time for different gas flow rates (M1 membrane)

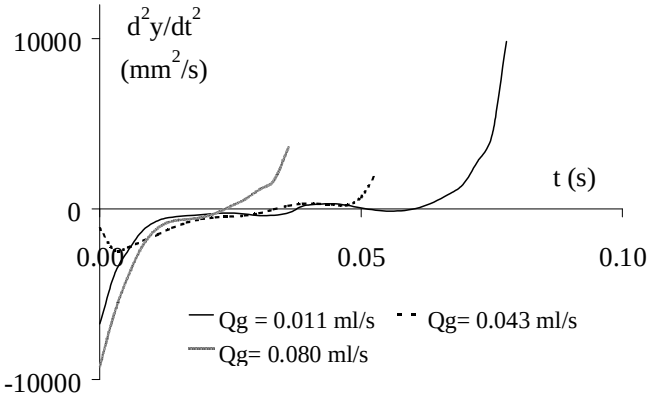

Fig.12. Vertical acceleration of the bubble centre of gravity versus formation time for different gas flow rates (M1 membrane)

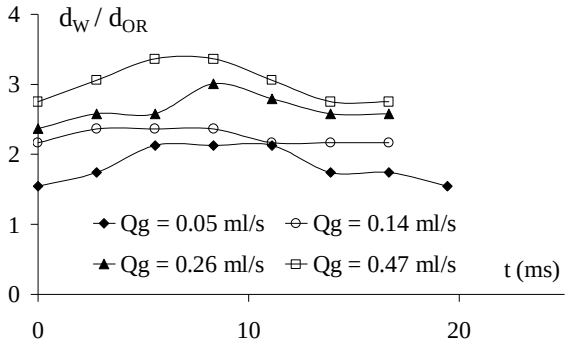

Fig.13. Ratio of surface/bubble contact diameter and hole diameter versus formation time for different gas flow rates (M4 membrane)

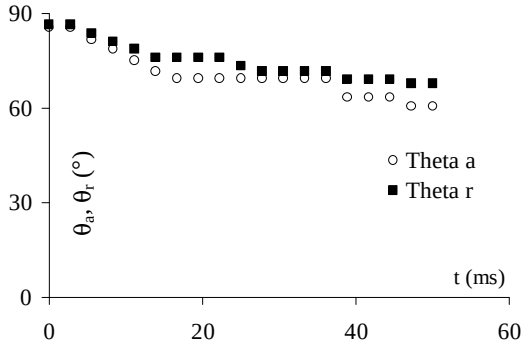

Fig.14. Contact angles versus formation time (M3 membrane Q_G=0.03 ml/s)

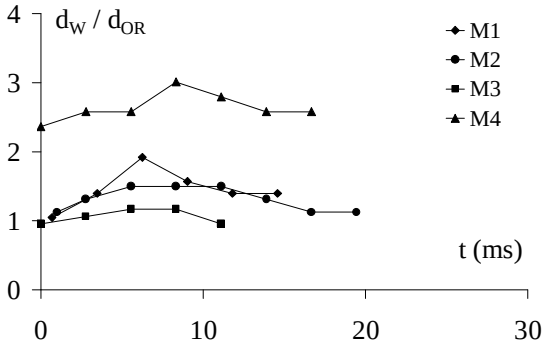

Fig.15. Ratio of surface/bubble contact diameter and hole diameter versus formation time for the four membranes (Q_G=0.26 ml/s)

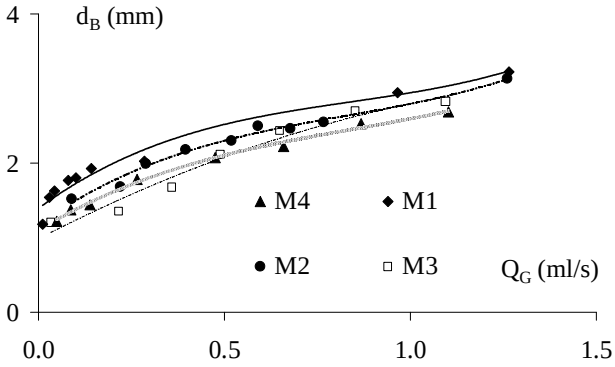

Fig.16. Bubble diameter versus gas flow rate

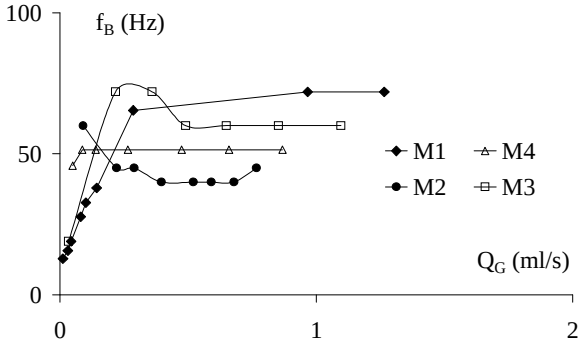

Fig.17. Bubble frequency versus gas flow rate

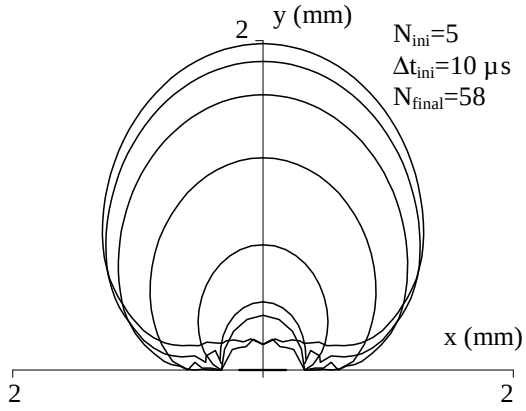

Fig.18. Bubble shape variation with time (Membrane M3; Q_G=0.49 ml/s

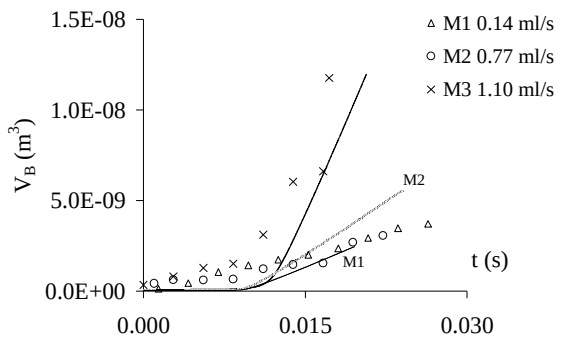

Fig.19. Calculated (continuous line) and experimental (symbols) bubble volume versus formation time

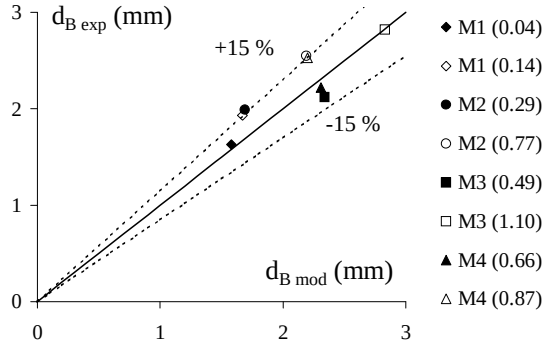

Fig.20. Comparison of experimental and calculated bubble diameter
[M_i≡membrane N°i (Q_G in ml/s])

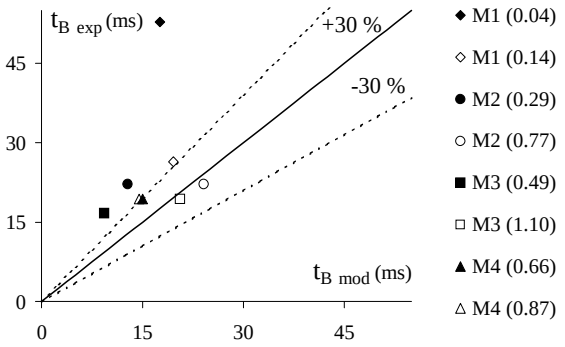

Fig.21. Comparison of experimental and calculated formation time
[M_i≡membrane N°i (Q_G in ml/s)]

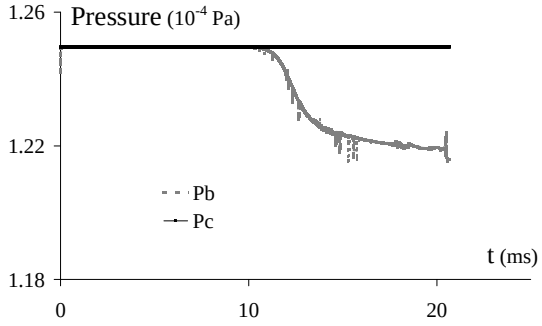

Fig.22. Calculated pressure changes in the bubble and in the gas chamber against bubble formation time (Membrane M3 Q_G=1.10 ml/s)

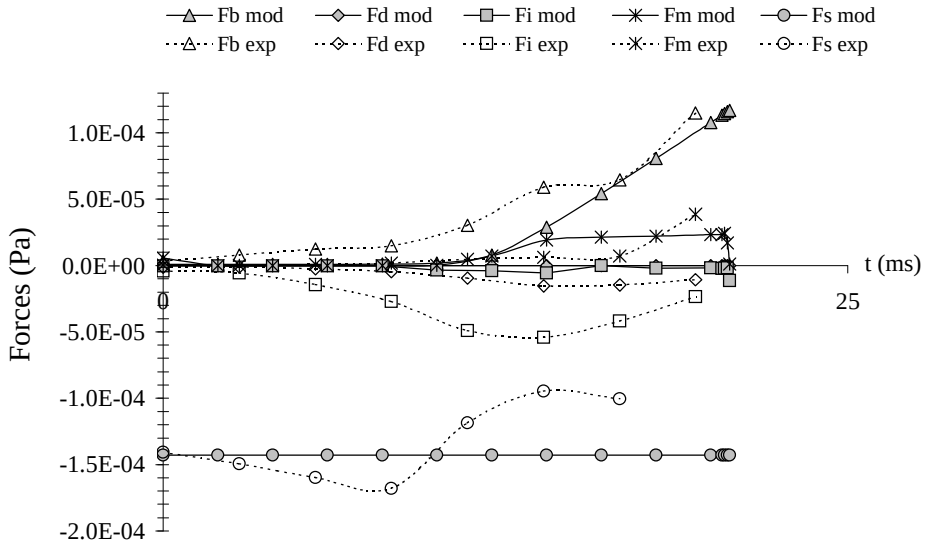

Fig.23. Variation in the experimental and the calculated forces acting on the bubble as a function of growth time (Membrane M3 Q_G=1.10 ml/s)

Table legend

Table 1: Bubble formation dimensionless numbers

Table 2: Geometrical and physical membrane characteristics

Table 3: Comparison of experimental data of Terasaka & Tsuge (1990) with results calculated by the present model

Membrane	Q_G (ml/s)	N_C	N_W	We
M1	0.01 – 2.53	163 - 66	0.04 – 6.6	$1.6.10^{-4}$ - 2
M2	0.09 – 0.77	219 - 185	0.32 – 2.6	0.016 – 0.91
M3	0.03 – 1.10	126 - 96	0.10 – 3.2	0.001 – 0.71
M4	0.05 – 0.87	602 - 426	0.22 – 3.6	0.021 - 4

Table 1: Bubble formation dimensionless numbers

Membranes	Thickness	γ_C	$f=\alpha.Re^{\beta}$		$T=K.\Delta P^n$		Δp_C	p_O
	(mm)	(mN/m)	α	β	K	n	(mbars)	(mbars)
M1	2.15	23	$1.71.10^6$	-1.47	0.22	0.81	115	104
M2	2.06	22	$6.3.10^4$	-1.42	0.22	0.81	35	22
M3	1.85	24	$3.3.10^5$	-1.49	1.84	0.60	63	55
M4	2.26	21	$6.3.10^4$	-1.45	0.17	0.83	45	27

Table 2: Geometrical and physical membrane characteristics

Liquid	V_C (m^3)	$t_{B\ modelling}$ (ms)	$t_{B\ experimental}$ (ms)	$d_{B\ modelling}$ (mm)	$d_{B\ experimental}$ (mm)
Distilled water	$4.25.10^{-5}$	39	40	6,6	5.7
ρ_L=997 kg/m^3; μ_L=$8.74.10^{-4}$ Pa.s	$9.75.10^{-5}$	45	47	6.9	7.5
σ_L=71.8 mN/m Q_G=$2.1.10^{-7}$ m^3/s	$3.005.10^{-4}$	63	56	9.1	9.6
Glycerol	$4.25.10^{-5}$	232	270	10	9.4
ρ_L=1260 kg/m^3; μ_L=1.11 Pa.s	$9.75.10^{-5}$	233	290	10.1	10.5
σ_L=62.2 mN/m Q_G=$1.1.10^{-6}$ m^3/s	$3.005.10^{-4}$	378	320	13.3	12.8

Table 3: Comparison of experimental data of Terasaka & Tsuge (1990) with results calculated by the present model: κ=1.1; H_L=0.2m; d_{OR}=1.47mm; k_{OR}=$1.76.10^{-6}m^{7/2}.kg^{-1/2}$; C_D=f(Re) calculated by Yoo et al. (1997) correlation.